

# A portable imaging Mueller matrix polarimeter based on a spatio-temporal modulation approach: theory and implementation

Israel J. Vaughn<sup>a</sup>, Oscar G. Rodríguez-Herrera<sup>b</sup>, Mohan Xu<sup>a</sup>, J. Scott Tyo<sup>a,c</sup>

<sup>a</sup>College of Optical Sciences, University of Arizona, Tucson, USA;

<sup>b</sup>Centro de Ciencias Aplicadas y Desarrollo Tecnológico, Universidad Nacional Autónoma de México, Cd. Universitaria, Mexico

<sup>c</sup>University of New South Wales @ ADFA, Canberra, ACT, Australia

## ABSTRACT

Imaging polarimeters have been largely used for remote sensing tasks, and most imaging polarimeters are division of time or division of space Stokes polarimeters. Imaging Mueller matrix polarimeters have just begun to be constructed which can take data quickly enough to be useful. We have constructed a Mueller matrix (active) polarimeter utilizing a hybrid modulation approach (modulated in both time and space) based on a micropolarizer array camera and rotating retarders. The hybrid approach allows for an increase in temporal bandwidth (instrument speed) at the expense of spatial bandwidth (sensor resolution). We present the hybrid approach and associated reconstruction schemes here. Additionally, we introduce the instrument design and some preliminary results and data from the instrument.

**Keywords:** polarimetry, modulated polarimetry, linear systems, active polarimetry, Mueller matrix

## 1. INTRODUCTION

Recent advances in polarimetric instrument design<sup>1-5</sup> have facilitated *systematic* instead of *ad-hoc* designs for specific tasks using a linear systems framework. Particularly Alenin and Tyo<sup>4</sup> have provided a general framework to design any periodically modulated polarimetric instrument. We utilized this framework to design an active polarimeter optimized for temporal bandwidth. The specific instrument presented here is designed optically for general remote sensing purposes at the 10 – 200m range. One motivating example of the need for more temporal bandwidth is skin cancer detection, in 2011 our group began evaluating combined hyperspectral and polarization measurements for utility in skin cancer and skin interaction.<sup>6</sup> A significant issue with our instrumentation was the requirement for image registration due to patient movement, and a great deal of effort was expended on improving image registration performance.

Faster instruments minimize the need for complex image registration algorithms and processing. In addition to mitigating image registration, the linear systems framework allows designers to reduce channel crosstalk. Channel crosstalk is often the cause of "erroneous" polarization measurements and can be thought of as a theoretical limitation instead of a systematic "error." We will address channel crosstalk in detail in another communication. In this communication, we present a spatio-temporal system design as a linear system, we develop an instrument design based on the theory, and finally we demonstrate the actual system and related issues.

---

Send correspondence to IJV or JST

IJV: israel.vaughn@gmail.com

JST: S.Tyo@adfa.edu.au

## 2. FORMALISM AND CHANNELS

We use the Mueller-Stokes mathematical formalism here, as it is most commonly used in instrumental polarization and polarimeter design. This analysis is, however, agnostic to the formalism used, a coherence formalism<sup>7</sup> with periodic modulators could also be used and would have similar results. In the next sections, it should be kept in mind that modulations are done in some physical domain, they are periodic, i.e., a superposition of sinusoidal functions, and the "channels" are the resultant  $\delta$ -functions which ensue from the Fourier transform of the sinusoidal modulations.

### 2.1 Modulated Mueller formalism

The Stokes parameters are described by

$$\mathbf{s} = \begin{bmatrix} s_0 \\ s_1 \\ s_2 \\ s_3 \end{bmatrix} = \begin{bmatrix} \langle |E_x|^2 \rangle + \langle |E_y|^2 \rangle \\ \langle |E_x|^2 \rangle - \langle |E_y|^2 \rangle \\ 2 \operatorname{Re} \langle E_x E_y^* \rangle \\ 2 \operatorname{Im} \langle E_x E_y^* \rangle \end{bmatrix} = \begin{bmatrix} \bullet \\ \updownarrow \\ \times \\ \circ \end{bmatrix}, \text{ where } s_0 > 0, \quad s_0^2 \geq s_1^2 + s_2^2 + s_3^2 \quad (1)$$

where  $\langle \cdot \rangle$  denotes the time average,  $s_0$  is proportional to the total irradiance,  $s_1$  is proportional to the prevalence of horizontal ( $0^\circ$ ) over vertical ( $90^\circ$ ) polarization,  $s_2$  is proportional to the prevalence of  $+45^\circ$  over  $-45^\circ$  polarization, and  $s_3$  is proportional to the prevalence of right circular over left circular polarization.<sup>8</sup> Because optical sensors measure a quantity proportional to the time averaged Poynting vector, the phase information is lost, and only the incoherent time averaged polarization information can be obtained.<sup>7,8</sup>

For materials which can be described via linear optical interactions, we can use the Mueller-Stokes formalism. A Mueller matrix,  $\mathbf{M}$ , is a matrix which linearly transforms one set of Stokes parameters,  $\mathbf{s}_{\text{in}}$ , into another set of Stokes parameters,  $\mathbf{s}_{\text{out}}$ :

$$\mathbf{s}_{\text{out}} = \mathbf{M} \cdot \mathbf{s}_{\text{in}} \quad (2)$$

Notice that  $\mathbf{M} \in \mathbb{R}^{4 \times 4}$  but not every  $4 \times 4$  real valued matrix is a Mueller matrix due to the constraints in Eqn.1, see Gil<sup>9</sup> for details.

With an active, or Mueller matrix, polarimetric instrument, we must modulate in irradiance to infer the Mueller matrix of an object,  $\mathbf{M}(\mathbf{x})$ , where  $\mathbf{x} = [x \ y \ z \ t \ \sigma]^T$ . We can then rewrite Eqn. 2 to have Mueller matrices and Stokes parameters be functions of space, time, and wavelength or wavenumber. Eqn. 2 then becomes

$$\begin{bmatrix} s_{0,\text{out}}(\mathbf{x}) \\ s_{1,\text{out}}(\mathbf{x}) \\ s_{2,\text{out}}(\mathbf{x}) \\ s_{3,\text{out}}(\mathbf{x}) \end{bmatrix} = \begin{bmatrix} m_{00}(\mathbf{x}) & m_{01}(\mathbf{x}) & m_{02}(\mathbf{x}) & m_{03}(\mathbf{x}) \\ m_{10}(\mathbf{x}) & m_{11}(\mathbf{x}) & m_{12}(\mathbf{x}) & m_{13}(\mathbf{x}) \\ m_{20}(\mathbf{x}) & m_{21}(\mathbf{x}) & m_{22}(\mathbf{x}) & m_{23}(\mathbf{x}) \\ m_{30}(\mathbf{x}) & m_{31}(\mathbf{x}) & m_{32}(\mathbf{x}) & m_{33}(\mathbf{x}) \end{bmatrix} \cdot \begin{bmatrix} s_{0,\text{in}} \\ s_{1,\text{in}} \\ s_{2,\text{in}} \\ s_{3,\text{in}} \end{bmatrix} \quad (3)$$

where for simplicity we fix  $\mathbf{s}_{\text{in}}$ . Our detector then measures a quantity proportional to  $s_{0,\text{out}}(\mathbf{x})$ . For a Mueller matrix measuring instrument, we have an unknown object Mueller matrix,  $\mathbf{M}_{\text{obj}}(\mathbf{x})$ , and we write down the instrument equation which modulates Stokes parameters:<sup>10</sup>

$$\mathbf{s}_{\text{out}}(\mathbf{x}) = \mathbf{A}(\mathbf{x}) \cdot \mathbf{M}_{\text{obj}}(\mathbf{x}) \cdot \mathbf{G}(\mathbf{x}) \cdot \mathbf{s}_{\text{in}} \quad (4)$$

$$= \mathbf{A}(\mathbf{x}) \cdot \mathbf{M}_{\text{obj}}(\mathbf{x}) \cdot \mathbf{s}_{\mathbf{G}}(\mathbf{x}) \quad (5)$$

where  $\mathbf{G}(\mathbf{x})$ ,  $\mathbf{A}(\mathbf{x})$  are the generator and analyzer Mueller matrices respectively, known and modulated via the physical instrument. The generator modulation can then be thought of as only a Stokes parameter modulation,  $\mathbf{s}_{\mathbf{G}}(\mathbf{x})$ .

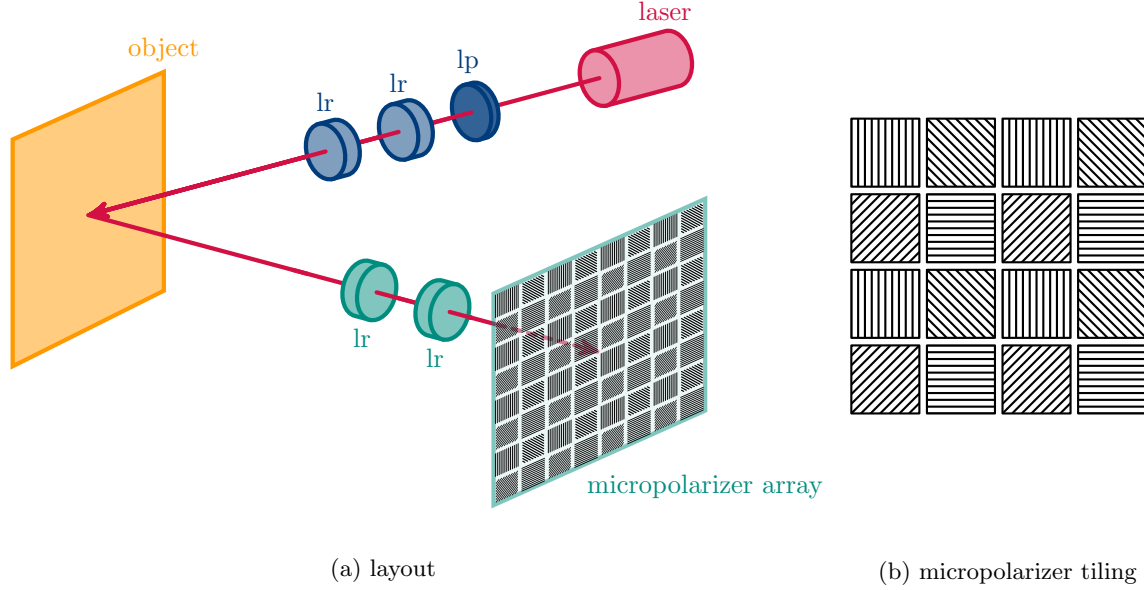


Figure 1: Spatio-temporally modulated polarimeter schematic, lp=linear polarizer, lr=linear retarder, blue components denote the polarization state generator (PSG), green components denote the polarization state analyzer (PSA). The micropolarizer array is the typical tiling, shown in (b). (a) was derived and modified from a figure created by Andrey Alenin.

## 2.2 Channels

Eqn. 5 can be expanded to obtain a linear equation<sup>8</sup> for  $s_{0,\text{out}}(\mathbf{x})$ .

$$s_{0,\text{out}}(\mathbf{x}) = \sum_{i=0}^3 \sum_{j=0}^3 a_{0i}(\mathbf{x}) s_j(\mathbf{x}) m_{ij}(\mathbf{x}) \quad (6)$$

where  $a_{0i}(\mathbf{x})$  are the elements of the first row of  $\mathbf{A}(\mathbf{x})$ ,  $s_j(\mathbf{x})$  are elements of  $\mathbf{s}_{\mathbf{G}}(\mathbf{x})$ , and  $m_{ij}(\mathbf{x})$  are elements of  $\mathbf{M}_{\text{obj}}(\mathbf{x})$ . We can then take the Fourier transform of  $s_{0,\text{out}}(\mathbf{x})$  to obtain

$$S_{0,\text{out}}(\boldsymbol{\rho}) = \sum_{i=0}^3 \sum_{j=0}^3 A_{0i}(\boldsymbol{\rho}) * S_j(\boldsymbol{\rho}) * M_{ij}(\boldsymbol{\rho}) \quad (7)$$

Where  $\mathbf{x} \rightarrow \boldsymbol{\rho}$  in the Fourier transform,  $*$  denotes convolution, and the shift to capital letters indicates a function has been Fourier transformed. If  $a_{0i}(\mathbf{x})$  and  $s_j(\mathbf{x})$  are superpositions of sinusoidal functions, then  $A_{0i}(\boldsymbol{\rho}) * S_j(\boldsymbol{\rho})$  is a set of  $\delta$ -functions, and each  $M_{ij}(\boldsymbol{\rho})$  is then convolved with each  $\delta$ -function in the set. The complete set of  $\delta$ -functions for the system

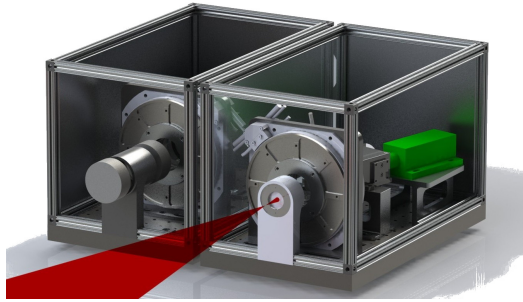
$$\sum_{i=0}^3 \sum_{j=0}^3 A_{0i}(\boldsymbol{\rho}) * S_j(\boldsymbol{\rho}) \quad (8)$$

are defined as the *channels* of the system, or the system's *channel structure*.<sup>4</sup>

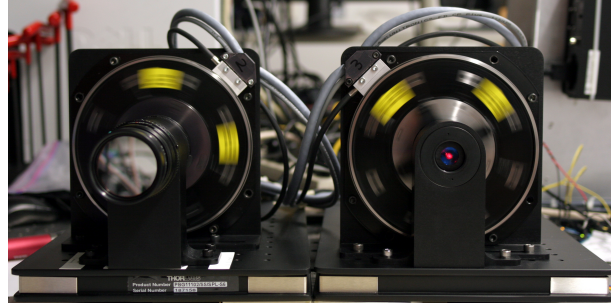
## 3. SPATIO-TEMPORAL INSTRUMENT DESIGN

Our group has had a need for an active portable polarimeter for some time, with the following capabilities:

- General remote sensing tasks, including multi-class detection



(a) Spatio-temporal design



(b) Actual Instrument

Figure 2: Hybrid Domain Modulated Imaging Polarimeter (HyDMIP)

- Data acquisition for supervised learning in detection tasks
- Validation of channeled polarimeter theory
- General data collection, with capability to access any Stokes parameter state for both generator and analyzer
- Fast and portable

The instrument presented here was not designed from the ground up as a channeled system, it began as a portable system that could potentially test some aspects of channeled systems while still meeting the other capabilities listed above as a general research instrument. This large set of general priorities resulted in an initial design consisting of a micropolarizer array camera and 4 rotating retarders. This design would meet all of the capabilities while still allowing us to validate channeled designs.

The initial design was specified to be spectrally broadband from  $635 - 830nm$ , however cost constraints forced us to design only the full Stokes polarization state analyzer (PSA) to be broadband, and the polarization state generator (PSG) to be narrowband at  $671nm$ . This allows for the PSA to be operated as a broadband portable full Stokes polarimeter by itself, or as a narrowband active Mueller matrix polarimeter when combined with the PSG. The PSG is a typical rotating retarder design,<sup>11</sup> with the polarization components placed in a collimated optical space, the only difference is that we use two rotating retarders instead of one. The PSA is a spatio-temporally modulated hybrid channeled system. The micropolarizer array provides spatial modulation,<sup>3,5,12</sup> and two rotating retarders provide temporal modulation. The retarders are in a collimated optical space. We call this polarimeter the Hybrid Domain Modulated Imaging Polarimeter (HyDMIP). See appendix A for more details.

Table 1: System specifications

	Component	Type	Detail
PSG	source	671nm laser	200mW
PSG	retarder(s)	671nm	1in dia.
PSG	stages(s)	up to 1000rpm	< 15arc sec accuracy
PSG	optics	aplanatic @ 633nm	matched to PSA FOV
PSA	sensor	silicon 1MP array @ 28.4 fps	9μm pixels, micropolarizer array
PSA	retarder(s)	630 – 835nm	2in dia.
PSA	stages(s)	up to 1000rpm	< 15arc sec accuracy
PSA	optics	afocal section for retarders	f/2.4

### 3.1 System equation

Using the Mueller-Stokes formalism, the system designed above can be described by the following equation:

$$\mathbf{s}_{\text{out}} = \mathbf{P}(x, y) \cdot \mathbf{R}(\nu_4, \epsilon_4, \delta_4) \cdot \mathbf{R}(\nu_3, \epsilon_3, \delta_3) \cdot \mathbf{M}_{\text{obj}}(x, y, t) \cdot \mathbf{R}(\nu_2, \epsilon_2, \delta_2) \cdot \mathbf{R}(\nu_1, \epsilon_1, \delta_1) \mathbf{s}_{\text{in}} \quad (9)$$

where

$$\mathbf{P}(x, y) = \text{micropolarizer array Mueller matrix} \quad (10)$$

$$\mathbf{R}(\nu_j, \epsilon_j, \delta_j) = \text{retarder Mueller matrix} \quad (11)$$

$$\nu_j = \text{retarder frequency in } 2\pi \frac{\text{radians}}{\text{s}} \quad (12)$$

$$\epsilon_j = \text{retarder start position in } 2\pi \text{ radians} \quad (13)$$





$$\delta_j = \text{retarder retardance in radians} \quad (14)$$

$$\mathbf{M}_{\text{obj}}(x, y, t) = \text{Mueller matrix of the object} \quad (15)$$

The first element of  $\mathbf{s}_{\text{out}}$ ,  $s_{0,\text{out}}$  is then sampled by the camera's focal plane array (FPA). Note that each  $\nu_j$  is implicitly dependent on time,  $t$ . We can then Fourier transform a 3-dimensional,  $(x, y, t)$  acquired data cube to retrieve the convolved data. For details see Alenin and Tyo<sup>4</sup> or Vaughn *et al.*<sup>13</sup>

## 4. CHANNEL DESIGN

Table 2: Notation for channels.

	positive	negative
real		
imag.		

Although HyDMIP is designed as a multipurpose instrument, in this communication we focus on using HyDMIP as a fast portable active polarimeter. This requires a channeled system design, given the constraints of our quad-retarder + micropolarizer instrument. The channels for HyDMIP were optimized using the free parameters available;  $\nu_1, \dots, \nu_4, \epsilon_1, \dots, \epsilon_4, \delta_1, \dots, \delta_4$ . More details about the optimization process are addressed in our other paper in this conference.<sup>13</sup> The optimization process yielded

$$\begin{aligned} \delta_1 &= \pi, & \delta_2 &= \pi - \arccos \frac{1}{\sqrt{3}}, & \delta_3 &= \pi - \arccos \frac{1}{\sqrt{3}}, & \delta_4 &= \pi \\ \nu_1 &= \frac{1}{2}, & \nu_2 &= -1, & \nu_3 &= 1, & \nu_4 &= \frac{1}{2} \end{aligned} \quad (16)$$

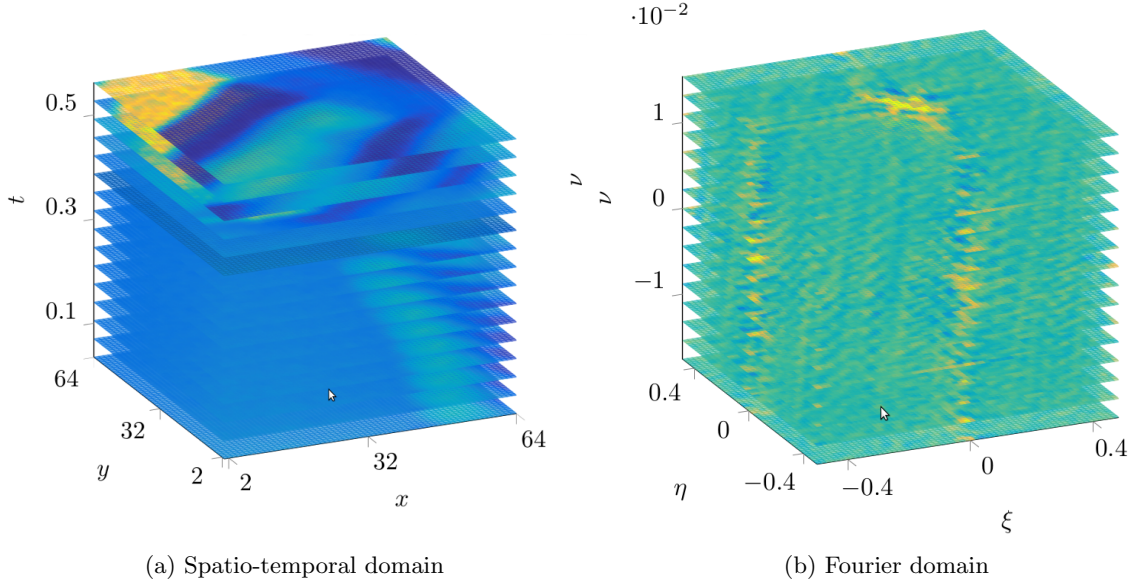


Figure 3: Space-time  $(x, y, t)$  modulated data cube transformed into Fourier domain.

up to a scaling constant for the  $\nu_j$ s, and irrespective of the  $\epsilon_j$ s. In the following analysis and results, however,  $\delta_2 = \frac{\pi}{2}$  due to retarder availability. This corresponds to the set of retarders actually used in the instrument. Fig. 4 shows the optimized channel structure for  $m_{23}$ . Note the triangles, the notation of which is explained in table 2. The size of the triangles corresponds to the magnitude of the respective  $\delta$ -function. Each  $\delta$ -function has an associated triangle which represents the complex scalar magnitude of that  $\delta$ -function.

As Alenin and Tyo have shown<sup>4</sup> (and Azzam<sup>11</sup> for the specific case of a temporally modulated system which assumes zero temporal bandwidth in the object), Mueller matrix reconstruction can be directly accomplished in the Fourier domain using the pseudoinverse of the  $\mathbf{Q}$  matrix,  $\mathbf{Q}^+$ . The effect of changing the retardance of the second retarder of the PSG,  $\delta_2$ , to be  $\frac{\pi}{2}$  has no effect on the bandwidth of the system, but results in a  $\mathbf{Q}$  matrix which isn't as well conditioned as in the optimal case. For our instrument this results in an increased effect of noise on reconstruction when compared with the optimal case.

## 5. RECONSTRUCTION

Conceptually, in a channeled system with measurements of data that contain some information, with some bandwidth content, we can think of each Mueller matrix element as a function over the domain of measurement,  $m_{ij}(\mathbf{x})$ , with the domain for our specific instrument being  $\mathbf{x} = [x \ y \ t]^T$ . For the channeled measurements, we can take the Fourier transform of each  $m_{ij}(\mathbf{x})$ :

$$M_{ij}(\boldsymbol{\rho}) = \mathcal{F} \{m_{ij}(x, y, t)\}_{\mathbf{x} \rightarrow \boldsymbol{\rho}}; \quad \boldsymbol{\rho} = \begin{bmatrix} \xi \\ \eta \\ \nu \end{bmatrix} \quad (17)$$

then the channeled system will convolve each  $M_{ij}(\boldsymbol{\rho})$  with the set of  $\delta$ -functions in the channel structure, resulting in a *mixture of data* in the Fourier domain. The exact mixing is characterized by the  $\mathbf{Q}$  matrix,<sup>4</sup> and we can unmix by using the pseudoinverse,  $\mathbf{Q}^+$ . Note that due to differences between the ideal channel structure, and the actual channel structure of an instrument which requires calibration,  $\mathbf{Q}$  must be determined via a *semi-empirical process*.

Additionally, the bandwidth extent of each  $M_{ij}(\boldsymbol{\rho})$  is formally determined by where  $M_{ij}(\boldsymbol{\rho}) \neq 0$ , with most real objects having infinite bandwidth. In practice, a filter can be determined or applied (hopefully) for  $|M_{ij}(\boldsymbol{\rho})| > \epsilon_c$  where  $\epsilon_c$  is some cut off threshold. The filter can then attenuate  $M_{ij}(\boldsymbol{\rho})$  over some subdomain of  $\boldsymbol{\rho}$ . If  $|M_{ij}(\boldsymbol{\rho})| >$

$\epsilon_c$  when  $\rho$  is outside of the range surrounding a channel for bandlimited reconstruction, then we have *channel crosstalk*.

### 5.1 Calibration

Actual instruments, of course, differ from ideal models. Our channel structure optimization assumed perfect polarizers, retarders, etc. This gave us a good design to first order, but calibration is needed to validate the bandwidth achievable and also to compute a proper  $Q$  matrix.<sup>4</sup> The  $Q$  matrix is computed with the semi-empirical model described below.

#### 5.1.1 Semi-empirical model

The first step of calibration was calibrating the micropolarizer array. This calibration was accomplished in a non-imaging setup by 1) placing white paper in front of a rotatable polarizer as a diffuser, which was then placed in front of the micropolarizer array and masked off for stray light, 2) rotating the polarizer with  $1^\circ$  increments and recording an image frame at each increment, 3) fitting a Malus' like law to each micropolarizer pixel and recording the parameters. The Malus' like law is

$$f(a, b, \theta') = a + b \cdot \cos^2(\theta + \theta') \tag{18}$$

where  $\theta$  is the rotation angle of the reference polarizer and  $\theta'$  is the angle of the micropolarizer of the pixel with respect to the lab reference frame (set by the reference polarizer). The extinction ratio can then be estimated

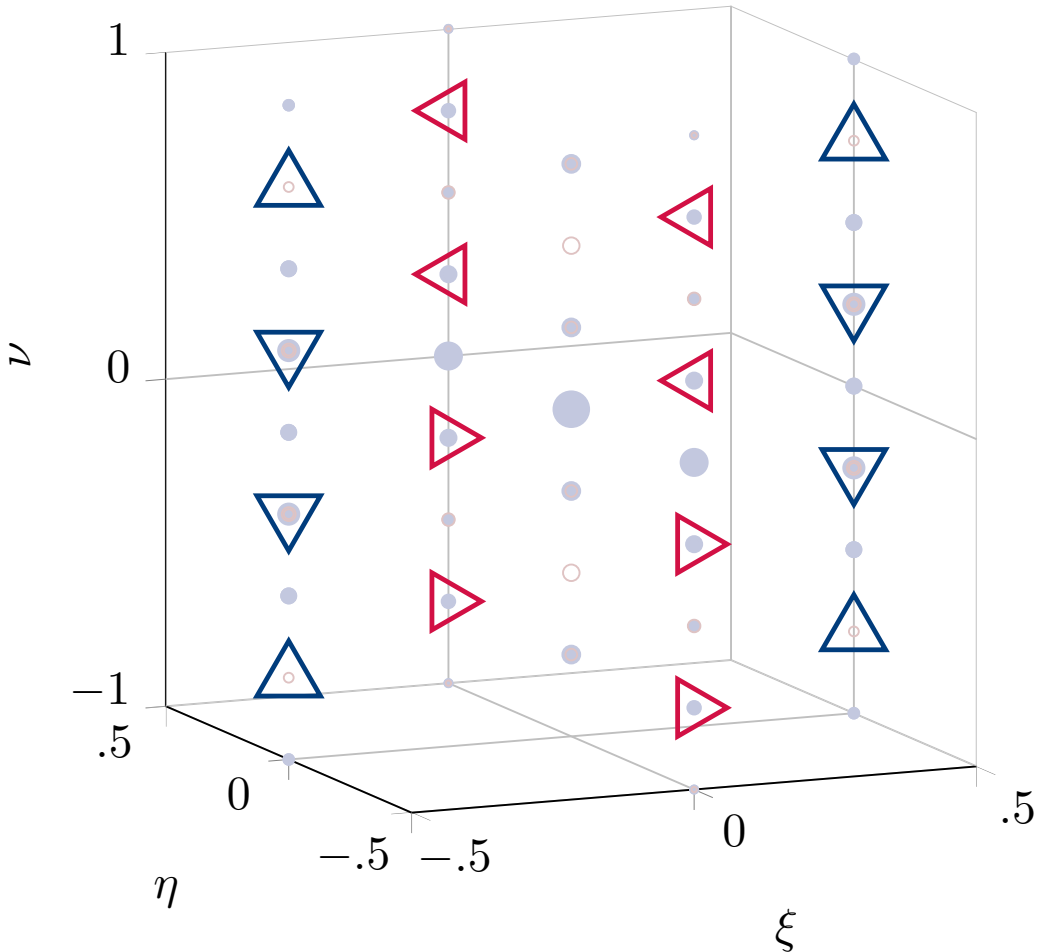


Figure 4: Optimized channel structure showing  $\delta$ -functions specific to  $m_{23}$

by either using the actual data for each pixel, or by

$$ER = \frac{a}{a + b} \quad (19)$$

note that the above doesn't account for dark current. If bad pixels are eliminated, our extinction ratios range from about 1 : 10 to 1 : 50, with the mean at  $\sim 1 : 17$ . These ratios were calculated directly from the data. The Malus' like law parameter fits for each pixel are then used as inputs for Mueller matrices of diattenuators.

The actual bulk retardances of each retarder are then used in the model, this is a valid assumption since the retarders are in collimated optical spaces and therefore the retardance doesn't have any significant spatial variation at the object or image planes. Finally, sampling at the correct framerate is implemented into the model. The model was designed to address Johnson (Gaussian like) detector noise and the remaining systematic error of retarder position wander during rotation. The Stokes parameters at each pixel,  $(x_k, y_l)$  are then computed at each time step,  $t_m$  as follows:

$$\begin{aligned} \mathbf{s}_{\text{out}}(x_k, y_l, t_m) = & \mathbf{P}(x_k, y_l) \cdot \mathbf{R}(\nu_4(t_m), \epsilon_4, \delta_4) \cdot \mathbf{R}(\nu_3(t_m), \epsilon_3, \delta_3) \\ & \cdot \mathbf{M}_{\text{test}} \cdot \mathbf{R}(\nu_2(t_m), \epsilon_2, \delta_2) \cdot \mathbf{R}(\nu_1(t_m), \epsilon_1, \delta_1) \mathbf{s}_{\text{in}} \end{aligned} \quad (20)$$

where

$$\mathbf{s}_{\text{in}} = \begin{bmatrix} 1 \\ -1 \\ 0 \\ 0 \end{bmatrix}, \text{ due to the laser polarization orientation} \quad (21)$$

and  $\mathbf{M}_{\text{test}}$  is a matrix with one element at  $0 \leq i, j \leq 3$  equal to 1 and all other elements zero. This gives the channel response of each specific Mueller matrix element. Each response for each time step and each pixel is then assembled into a 3-dimensional data cube and Fourier transformed. The channel weights can then be read off to assemble the  $\mathbf{Q}$  matrix.

## 5.2 Inversion

After the  $\mathbf{Q}$  matrix is computed from the semi-empirical model, then data can be acquired and inverted to obtain Mueller matrix images. The inversion process is outlined below:

- Acquire data (image stack sampled at evenly spaced time points)
- Compute 3-dimensional Fourier transform of acquired data cube
- Filter data around each channel site (for our case we will get 23 smaller data cubes)
- Apply the pseudoinverse,  $\mathbf{Q}^+$  in the Fourier domain elementwise to obtain a Fourier representation of each Mueller matrix element.
- Inverse Fourier transform the Fourier representation of each element to obtain a spatio-temporally resolved data cube for each Mueller matrix element.
- Display the Mueller matrix images (over time if needed).

There are some additional steps which are glossed over here, for example since we are sampling at the Nyquist frequency in both time and space, we have to use Hermiticity conditions to fully reconstruct filtered data on the edges of the data cube, which is error prone to implement in 3-dimensions. Fig. 5 shows an example of filtered data in the Fourier domain from the actual instrument.

Our specific system also has some constraints that weren't apparent at the outset of the design. Since we are discretely sampling, and we want to build a fast instrument, we must assume that we can know our channels, and hence  $\mathbf{Q}$  *a priori*. Due to spectral leakage (which we won't delve into here) this system requires Fourier



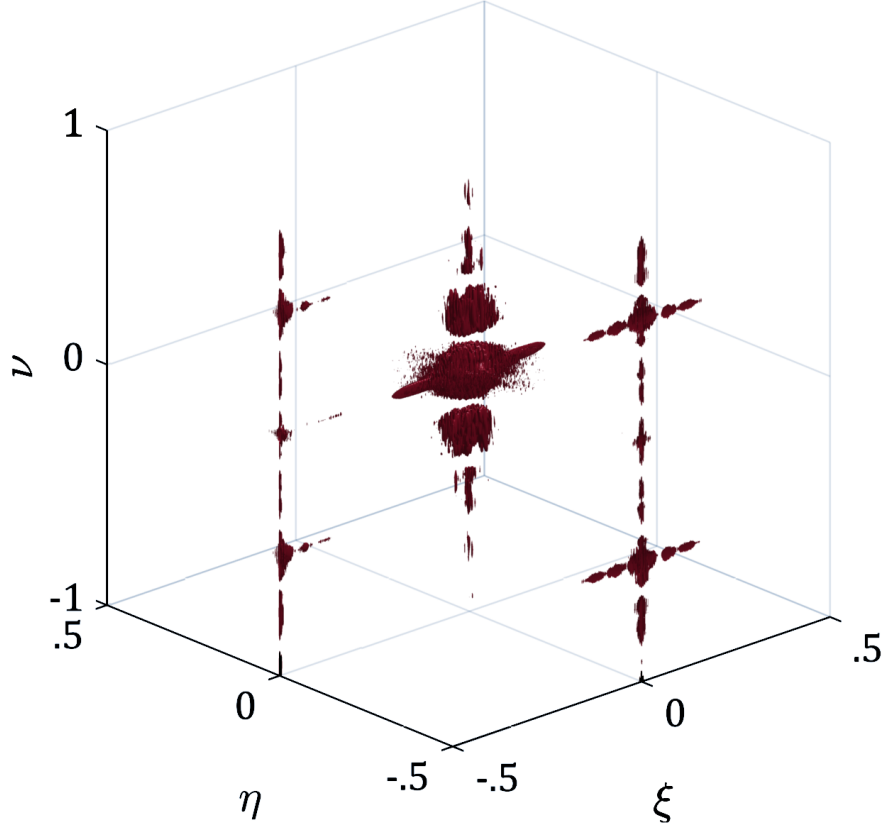


Figure 5: Filtered data from HyDMIP in the Fourier domain.

transforms occur on a time window which is a multiple of 8 frames wide, and must be greater or equal to 16 frames wide. This forces a minimum time lag of

$$\frac{8}{R} \text{ where } R \text{ is the camera frame rate in frames per second.} \quad (22)$$

Our system has a camera operating at  $28.4fps$  which corresponds to a minimal lag of  $282ms$ . This implies that whatever is happening in the scene now won't show up in the Mueller matrix images until  $282ms$  later. This isn't a huge lag, but could be an issue for some applications.

## 6. RESULTS

Our instrument was very recently completed, so the results presented here are preliminary. First, we will discuss some issues that we could not overcome prior to publication, but we are confident that our design and analysis are still valid. We shall then present some results which illustrate the channel crosstalk issue.

### 6.1 Validation

After initial data collection and inversion of that data using the  $Q^+$  derived from the semi-empirical model, it was clear that the actual  $Q_{inst}$  of our instrument and the derived  $Q_{se}$  from our semi-empirical model did not match. We noticed this because some measured Mueller matrix images appeared to be physically incorrect. Fig. 6 elucidates the issue clearly, the left hand panel shows the channels from our semi-empirical model with a linear polarizer as an object, and the right hand panel shows the channels from an actual polarizer measured with the instrument. We have made some consistency checks and have validated most of the model assumptions, but the following discrepancies could be causing the difference:

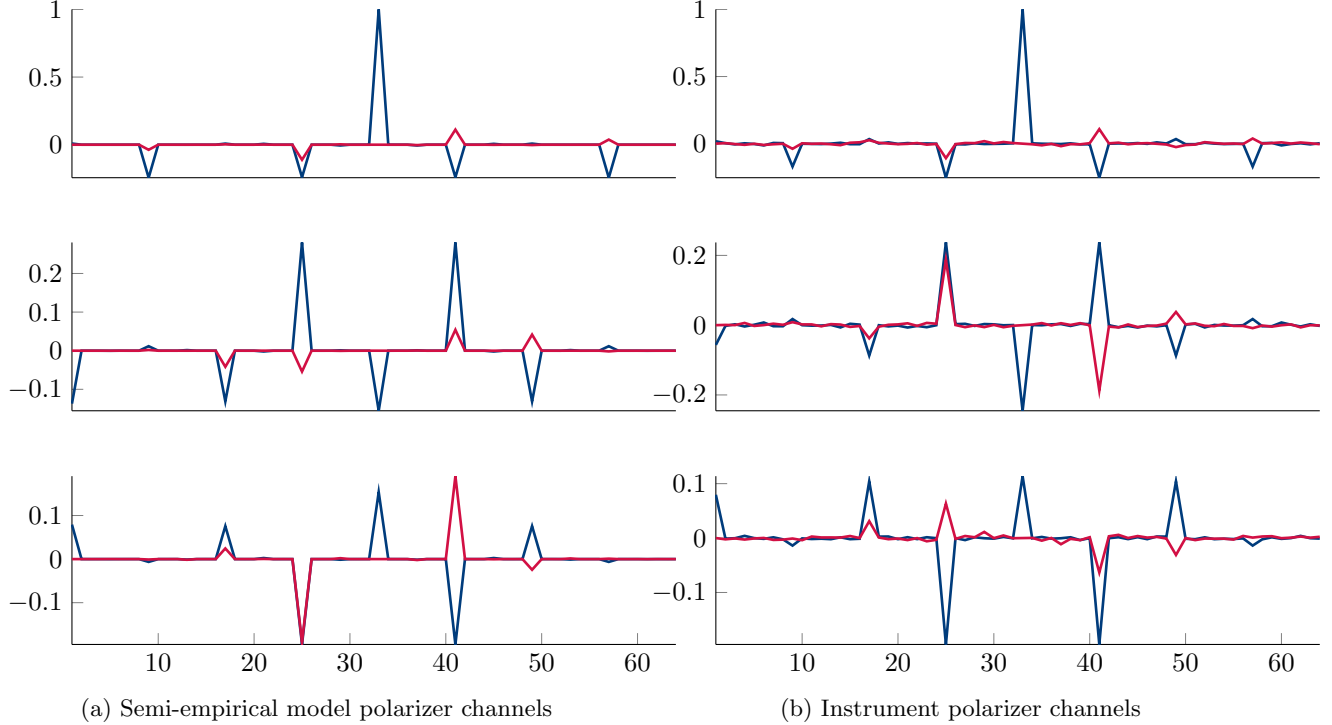


Figure 6: Difference between our semi-empirical model and measured data for the channel structure when a linear polarizer oriented at  $0^\circ$  is present.

- Rotation of the focal plane array between the real instrument and the model.
- Misalignment between the in plane axis of the PSG and the focal plane array.
- Missed frame or trigger causing a time shift between our model and the actual instrument.
- Stage offsets are incorrect (although we have repeatedly verified that they are correct).
- Model coordinate frame is otherwise rotated from the actual instrument coordinate frame.
- $\mathbf{s}_{\text{in}}$  is rotated from our assumptions in the actual instrument.
- Coordinate frame definitions are inconsistent between the model and the actual instrument.
- Gap between the micropolarizer array and FPA (this can be investigated by changing the  $f/\#$ )<sup>14</sup>

Qualitatively, Fig. 6 indicates that we are close to the correct  $\mathbf{Q}$  matrix, and even though the inversion  $\mathbf{Q}^+$  isn't quite correct at the moment, the bandwidth and crosstalk effects are still relevant. The channels are all in the right position, which means channel bandwidth and crosstalk can be demonstrated.

## 6.2 Bandwidth and crosstalk

The theory behind crosstalk and implications for this instrument are discussed elsewhere,<sup>13</sup> but we show crosstalk effects from actual data here. Briefly, channel crosstalk occurs when high frequency data from an one channel "bleeds" into an adjacent channel. There is no way to "unmix" the high frequency data which "bled over" from the data at the adjacent channel(s) to the current channel. This fact arises because for a general object, there is no way to know, *a priori*, what the data frequency content of that object will be.

Fig. 7 shows an image of  $m_{01}$  reconstructed from actual instrument data (shown in Fig. 5). In this data acquisition we manually rotated a glass plate at different speeds. The image shown is reconstructed from data

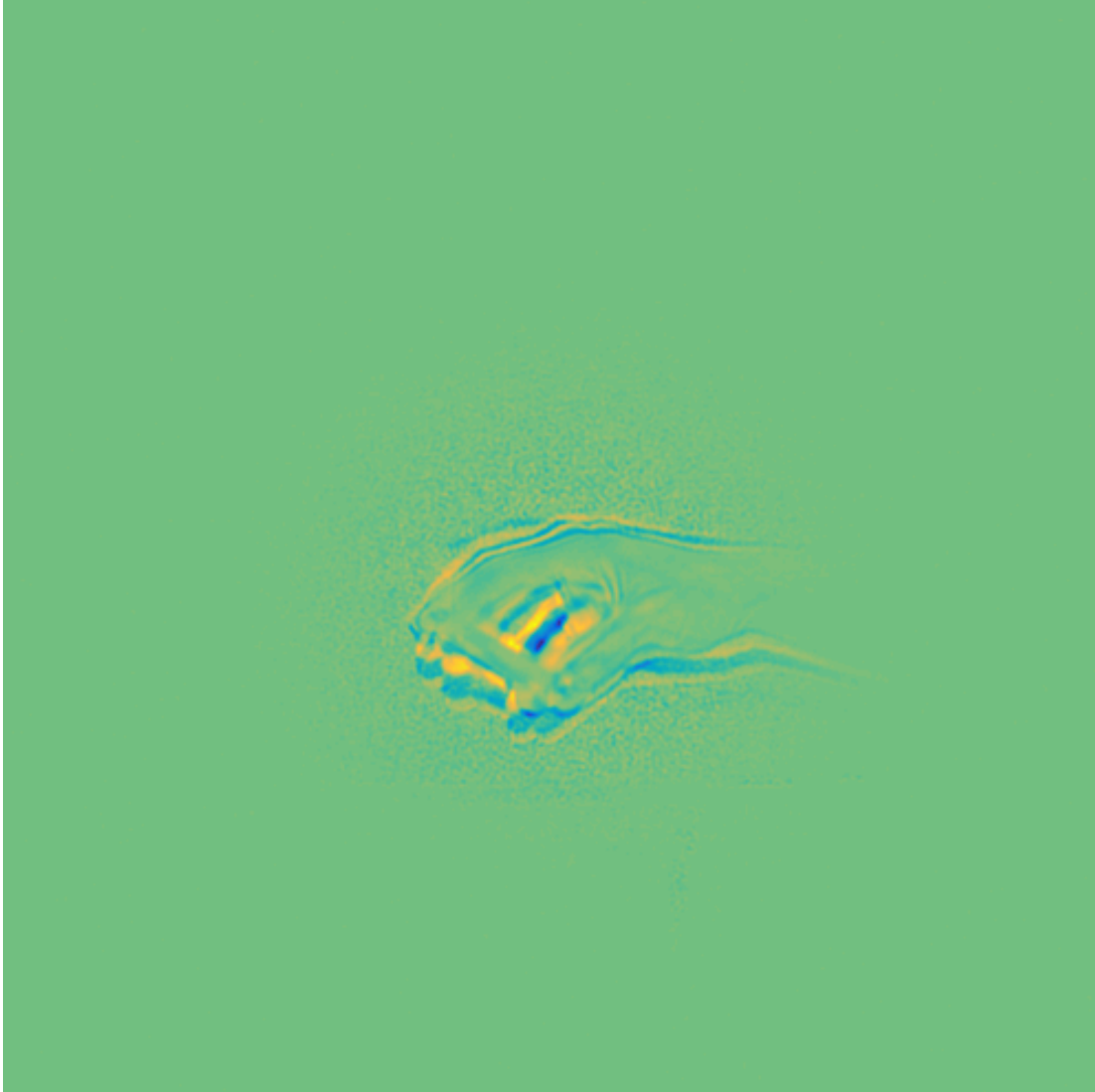


Figure 7: Reconstructed movement of hand and glass plate for  $m_{01}$ , notice the “artifacts” due to channel crosstalk.

where the plate was moving quite fast, and “artifacts” can be seen around the edges of the hand holding the plate. These “artifacts” are a result of channel crosstalk, and cannot be completely mitigated given a fixed camera acquisition rate.

### 6.3 Performance

We believe that we have designed and built one of the fastest (if not the fastest) portable Mueller matrix imaging polarimeters to date, and we hope to soon have a deployable instrument to collect data for remote sensing detection tasks. Our polarimeter can reconstruct full Mueller matrix images at a rate of  $1/8$  of the base camera rate, e.g., for a  $30fps$  camera, we can accomplish a Mueller matrix imaging rate of  $3.75fps$ . For comparison, a typical dual rotating retarder Mueller matrix polarimeter (which is temporally modulated only) can attain a rate of  $1/24$  of the base camera rate, resulting in a Mueller matrix image rate of  $1.25fps$  for a camera operating at  $30fps$ . However, because our polarimeter exploits a tradeoff between spatial image resolution and temporal bandwidth, we only attain Mueller matrix images with  $1/4$  of the resolution of the base camera.

## 7. CONCLUSION

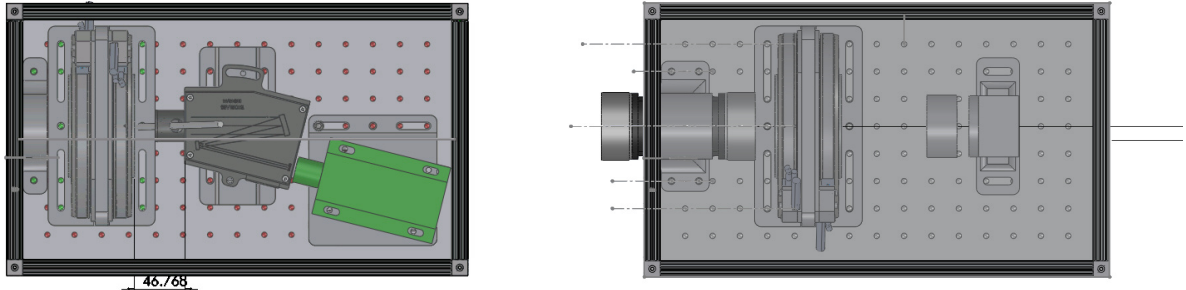
We have demonstrated the design and implementation of a portable imaging Mueller matrix polarimeter, HyD-MIP, and we believe that it is the fastest imaging Mueller matrix polarimeter built to date. The design relied on the general linear systems framework introduced by Alenin and Tyo<sup>4</sup> to optimize our instrument for temporal bandwidth in a systematic way, given our constraints and specifications. Our actual instrument appears to perform close to what we would expect given the theory, but there are some discrepancies between our instrument and our semi-empirical instrument model. These discrepancies will have to be addressed before the instrument can be deployed to the field to collect data for detection tasks.

### 7.1 Future work

Finalizing the instrument design and implementation includes fixing the semi-empirical model, writing software to reconstruct Mueller matrix images in “real time,” (re-)calibrating the entire system via known polarimetric elements, ensuring camera triggers aren’t missed, and collecting data.

## APPENDIX A. INSTRUMENT DETAILS

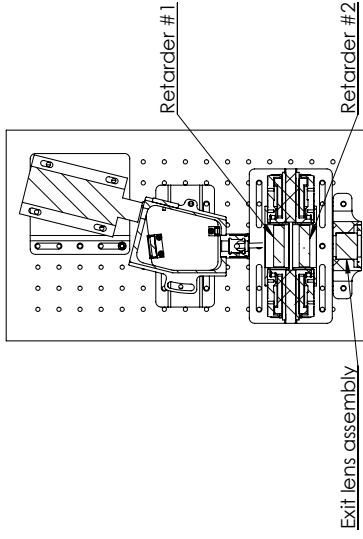
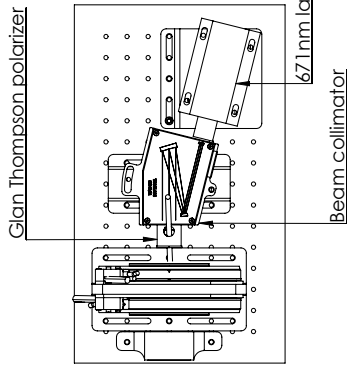
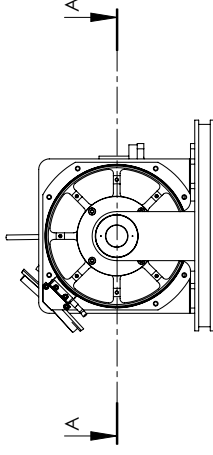
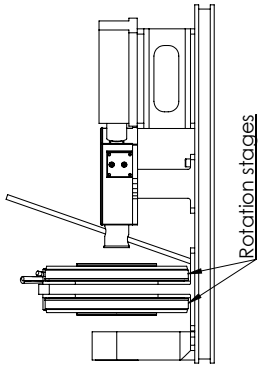
We include here some opto-mechanical details, the Source Assembly is the PSG, and the Receiver Assembly is the PSA. Fig 8 shows a top view of the instrument design.



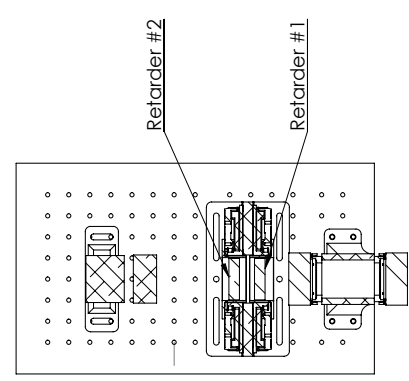
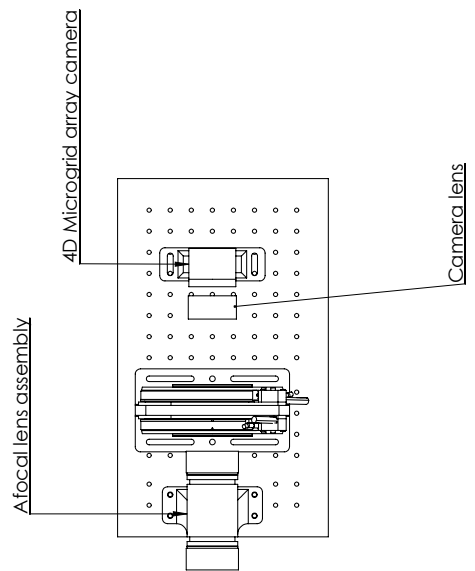
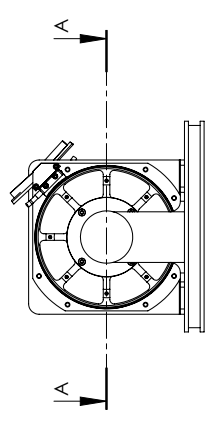
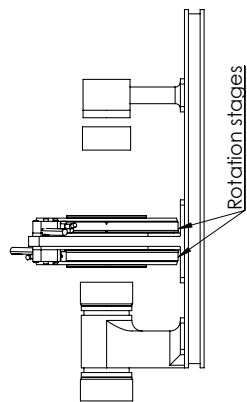
(a) Top view of PSG

(b) Top view of PSA

Figure 8: Renderings of the source and receiver for HyDMIP.



ALL UNTOLENCED BASIC DIMENSIONS DEFINED BY 0.01 A B C		DO NOT SCALE DRAWING UNIVERSITY OF ARIZONA, OPTICAL SCIENCES		Quantity : 1
ALL ANGLES $\pm 1^\circ$ UNLESS OTHERWISE SPECIFIED		DO NOT SCALE DRAWING UNIVERSITY OF ARIZONA, OPTICAL SCIENCES		REVISION 15
FINISH: 125/ ALL MACHINED SURFACES UNLESS OTHERWISE SPECIFIED		TITLE: Source Assembly		Part # A22
DRAWN CHECKED APPROVED INFG G.A.	NAME SIGNATURE DATE	MATERIAL: Mixed	SCALE: 1:3	SHEET 1 OF 1
WEIGHT ERROR/Weight		SCALE: 1:3		



SECTION A-A

ALL ANGLES $\pm 1^\circ$ UNLESS OTHERWISE SPECIFIED		ALL UNTOLERANCED BASIC DIMENSIONS DEFINED BY		Quantity : 1	
FINISH: 125/ ALL MACHINED SURFACES UNLESS OTHERWISE SPECIFIED		DO NOT SCALE DRAWING		REVISION 21	
UNIFORM AND BREAK SHARP EDGES .005-.0025 RADI .015-.10		University of Arizona, Optical Sciences		TITLE: Receiver Assembly	
NAME	SIGNATURE	DATE	Part #		
DRAWN			A23		
CHEK			A3		
APPVD			SCALE: 1.5		
MFG			SHEET 1 OF 1		
G.A.			Weight Error/Weight		
MATERIAL: Mixed					

## ACKNOWLEDGMENTS

The authors would like to thank Andrey Alenin for his insight and discussion about the design of this polarimetric instrument.

This work was supported by the Air Force Office of Scientific Research under award FA-9550-10-0114, the National Science Foundation under award DGE-0841234, and the University of Arizona TRIF Imaging Fellowship Program.

The hardware was procured through the Defense University Research Instrumentation Program under award FA-9550-12-1-0014.

## REFERENCES

- [1] Oka, K., “Singleshoot spectroscopic polarimetry using channeled spectrum,” in [*Photonics Asia 2002*], 167–175, International Society for Optics and Photonics (2002).
- [2] Kudenov, M. W., Escuti, M. J., Hagen, N., Dereniak, E. L., and Oka, K., “Snapshot imaging mueller matrix polarimeter using polarization gratings,” *Optics letters* **37**(8), 1367–1369 (2012).
- [3] LaCasse, C. F., Ririe, T., Chipman, R. A., and Tyo, J. S., “Spatio-temporal modulated polarimetry,” *Proc. SPIE* **8160**, 81600K–81600K–11 (2011).
- [4] Alenin, A. S. and Tyo, J. S., “Generalized channeled polarimetry,” *J. Opt. Soc. Am. A* **31**, 1013–1022 (May 2014).
- [5] LeMaster, D. A. and Hirakawa, K., “Improved microgrid arrangement for integrated imaging polarimeters,” *Opt. Lett.* **39**, 1811–1814 (Apr 2014).
- [6] Alenin, A. S., Morrison, L., Curiel, C., and Tyo, J. S., “Hyperspectral measurement of the scattering of polarized light by skin,” in [*SPIE Optical Engineering+ Applications*], 816014–816014, International Society for Optics and Photonics (2011).
- [7] Wolf, E., [*Introduction to the Theory of Coherence and the Polarization of Light*], Cambridge University Press, New York, United States (2007).
- [8] Collett, E., “Polarized light. fundamentals and applications. 1993.”
- [9] Gil, J. J., “Characteristic properties of mueller matrices,” *Journal of the Optical Society of America A* **17**, 328–334 (2000).
- [10] Chipman, R., “Handbook of optics: Volume i: Geometrical and physical optics, polarized light, components and instruments,” (2009).
- [11] Azzam, R. M. A., “Photopolarimetric measurement of the mueller matrix by fourier analysis of a single detected signal,” *Opt. Lett.* **2**, 148–150 (Jun 1978).
- [12] LaCasse, C. F., Chipman, R. A., and Tyo, J. S., “Band limited data reconstruction in modulated polarimeters,” *Opt. Express* **19**, 14976–14989 (Aug 2011).
- [13] Vaughn, I. J., Rodríguez-Herrera, O. G., Xu, M., and Tyo, J. S., “Bandwidth and crosstalk considerations in a spatio-temporally modulated polarimeter,” *Proc. SPIE* **9613** (2015).
- [14] Myhre, G., Hsu, W.-L., Peinado, A., LaCasse, C., Brock, N., Chipman, R. A., and Pau, S., “Liquid crystal polymer full-stokes division of focal plane polarimeter,” *Opt. Express* **20**, 27393–27409 (Dec 2012).